AGU PUBLICATIONS

JGR

Journal of Geophysical Research: Oceans

RESEARCH ARTICLE

10.1002/2015JC011378

Key Points:

- ANCP in shelf and coastal regions is up to 8 times higher than offshore regions
- ANCP in the seaward of shelf break shows high interannual variability
- ANCP interannual variability is associated with sea-ice dynamics and the SAM and ENSO climate indices

Supporting Information:

- Supporting Information S1

Correspondence to:
Z. Li,
zuchuan.li@duke.edu

Citation:
Li, Z., N. Cassar, K. Huang, H. Ducklow, and O. Schofield (2016), Interannual variability in net community production at the Western Antarctic Peninsula region (1997–2014), *J. Geophys. Res. Oceans*, *121*, 4748–4762, doi:10.1002/2015JC011378.

Received 6 OCT 2015
Accepted 7 JUN 2016
Accepted article online 9 JUN 2016
Published online 10 JUL 2016

Interannual variability in net community production at the Western Antarctic Peninsula region (1997–2014)

Zuchuan Li[1], Nicolas Cassar[1], Kuan Huang[1,2], Hugh Ducklow[3], and Oscar Schofield[4]

[1]Division of Earth and Ocean Sciences, Nicholas School of the Environment, Duke University, Durham, North Carolina, USA, [2]Picarro Inc., Santa Clara, California, USA, [3]Lamont-Doherty Earth Observatory, Columbia University, Palisades, New York, USA, [4]Institute of Marine and Coastal Sciences, School of Environmental and Biological Sciences, Rutgers University, New Brunswick, New Jersey, USA

Abstract In this study, we examined the interannual variability of net community production (NCP) in the Western Antarctic Peninsula (WAP) using in situ O_2/Ar-NCP estimates (2008–2014) and satellite data (SeaWiFS and MODIS-Aqua) from 1997 to 2014. We found that NCP generally first peaks offshore and follows sea-ice retreat from offshore to inshore. Annually integrated NCP (ANCP) displays an onshore-to-offshore gradient, with coastal and shelf regions up to 8 times more productive than offshore regions. We examined potential drivers of interannual variability in the ANCP using an Empirical Orthogonal Function (EOF) analysis. The EOF's first mode explains $\sim$50% of the variance, with high interannual variability observed seaward of the shelf break. The first principal component is significantly correlated with the day of sea-ice retreat ($R = -0.58$, $p < 0.05$), as well as the Southern Annular Mode (SAM) and El Niño Southern Oscillation (ENSO) climate indices in austral spring. Although the most obvious pathway by which the day of sea-ice retreat influences NCP is by controlling light availability early in the growing season, we found that the effect of day of sea-ice retreat on NCP persists throughout the growing season, suggesting that additional controls, such as iron availability, are preconditioned or correlated to the day of sea-ice retreat.

1. Introduction

The Western Antarctic Peninsula (WAP) region of the Southern Ocean (refer to Appendix A for acronyms and abbreviations) has undergone significant climate change over recent decades [*Ducklow et al.*, 2007; *Vaughan et al.*, 2003]. Since 1950, the annual mean air temperature has increased by approximately 2°C and winter air temperature by about 6°C [*King*, 1994; *Vaughan et al.*, 2003], leading to an earlier sea-ice retreat and a later sea-ice advance [*Stammerjohn et al.*, 2008a, 2008b]. These environmental changes have resulted in a shift of phytoplankton from large diatoms toward small flagellated cryptophytes [*Montes-Hugo et al.*, 2009], variation in the abundance of Antarctic krill [*Steinberg et al.*, 2015], and a decline in Adélie penguins near Palmer Station [*Clarke et al.*, 2007; *Ducklow et al.*, 2007]. The extent to which these changes in sea-ice and ecosystem dynamics alter carbon export production remains unclear.

Several methods have been employed at the WAP to study carbon export production, including sediment traps [*Ducklow et al.*, 2008, 2006], ^{234}Th [*Buesseler et al.*, 2010], and ^{15}N methods [*Weston et al.*, 2013]. Alternatively, carbon export production can be indirectly estimated using the O_2/Ar method [*Huang et al.*, 2012; *Tortell et al.*, 2014]. The O_2/Ar method estimates biological oxygen (O_2) saturation based on the similar solubility properties of O_2 and argon (Ar). Multiplying the biological O_2 by a gas exchange velocity leads to an estimate of net community production (NCP) which is defined as the difference between net primary production (NPP) and heterotrophic respiration (HR). At steady state and when averaged over appropriate scales, NCP approximates carbon export production [*Brix et al.*, 2006; *Eppley and Peterson*, 1979; *Sarmiento and Gruber*, 2006].

The spatial and temporal resolution provided by the various in situ methods presented above is however not sufficient to characterize the seasonal cycle of carbon export production over the entire WAP region. On these spatial and temporal scales, NCP can be estimated based on empirical or mechanistic relationships between NCP and ocean-color parameters such as chlorophyll *a* concentration ([Chl]) and particulate

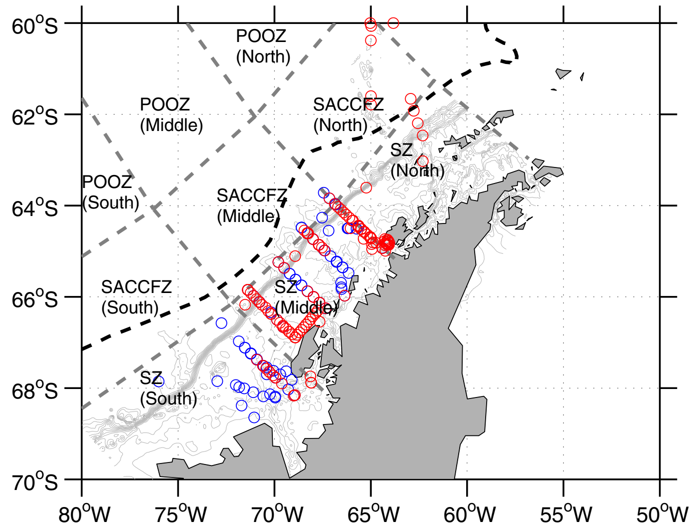

Figure 1. Study area (extended Pal-LTER region). Red and blue symbols represent the locations of in situ [Chl] samples matched to SeaWiFS and MODIS-Aqua observations, respectively. Heavy dashed line is the approximate location of the Southern Antarctic Circumpolar Front (SACCF) [*Orsi et al*., 1995]. Gray dashed line separates the WAP region into nine subregions. Thin gray lines represent 250 m-increment isobaths, which collapse into a thick gray line at the shelf break (750 m deep).

organic carbon concentration ([POC]) [*Cassar et al*., 2015; *Huang et al*., 2012; *Reuer et al*., 2007]. For example, *Chang et al*. [2014] and *Li and Cassar* [2016] recently estimated NCP for the Southern Ocean and the global oceans using in situ O_2/Ar-NCP estimates and various statistical methods including Artificial Neural Networks (ANNs), Support Vector Regression (SVR), and Genetic Programming (GP). Although these approaches estimate NCP relatively well, uncertainties remain significant, in part due to factors controlling NCP varying from one area to another. Some of these uncertainties can be reduced by developing regional algorithms.

In this study, we used satellite observations to investigate the mechanisms driving seasonal and interannual variability in NCP at the WAP. To that end, we first build a satellite-NCP algorithm specific to the WAP region. We develop an NCP-[Chl] regression using in situ [Chl] and O_2/Ar-NCP estimates. We derive a time series of monthly NCP (MNCP) and annually integrated NCP (ANCP), using the NCP-[Chl] regression and satellite-[Chl] algorithms specifically calibrated using in situ observations collected as part of the Palmer Long-Term Ecological Research (Pal-LTER) program [*Ducklow et al*., 2007]. Finally, we decompose ANCP into spatial (Empirical Orthogonal Function, EOF) and temporal (Principal Component, PC) components through an EOF analysis, and compare the temporal component to sea-ice dynamics, sea surface temperature (SST), photosynthetically active radiation (PAR), and the Southern Annular Mode (SAM) and El Niño Southern Oscillation (ENSO) climate indices.

2. Materials and Methods

2.1. Study Area

Our study area ranges from 60°S to 70°S in latitude and 80°W to 50°W in longitude (Figure 1). The area includes the Pal-LTER grid region which has been extensively investigated since 1990s [*Ducklow et al*., 2007]. Based on distance from the coast [*Martinson et al*., 2008], the study area was divided into a less productive Permanently Open Ocean Zone (POOZ) (>500 km), a relatively productive Southern Antarctic Circumpolar Current Front Zone (SACCFZ) (200–500 km) and a highly productive Shelf Zone (SZ) (<200 km) [*Smith et al*., 2008; *Treguer and Jacques*, 1992]. Offshore regions consist of POOZ and SACCFZ. Each region was further subdivided into southern (south of Pal-LTER grid line 250), middle (between Pal-LTER grid lines 250 and 600) and northern (between Pal-LTER grid lines 600 and 1000) sectors, leading to nine subregions. In order to detect secular trends in ANCP in the northern and southern regions, we divided the northern and middle sectors following *Montes-Hugo et al*. [2009], with the middle and southern sectors divided following *Smith et al*. [2008]. We defined the SACCFZ to be 100 km wider than *Smith et al*. [2008] so that regions with high ANCP variability were included in the SACCFZ (see section 3).

2.2. In Situ Measurements

In situ [Chl] measurements were collected during the annual Pal-LTER cruises in January and early February from 1993 to 2015. These measurements were downloaded from http://pal.lternet.edu/. Averaged [Chl] above a 10 m depth for each depth profile was matched to daily remote sensing reflectance just above water surface ($Rrs(\lambda)$), yielding match-ups of 145 and 99 for SeaWiFS and MODIS-Aqua, respectively (Figure 1). These match-ups were used to develop satellite-[Chl] algorithms specific to the WAP region.

Published and new O_2/Ar-NCP estimates collected between 2008 and 2014 were used to train our algorithms. Oxygen saturation reflects physical and biological processes. Because Ar has similar solubility properties to O_2, the ratio of O_2 and Ar (O_2/Ar) can be used to isolate the O_2 saturation associated with biological processes [*Craig and Hayward*, 1987; *Cassar et al*., 2011], from which NCP can be derived using a gas exchange rate parameterized as a function of wind speed [*Reuer et al*., 2007]. We matched our in situ mixed-layer-averaged [Chl] to O_2/Ar-NCP estimates to update the regression from *Huang et al*. [2012], yielding 175 match-ups.

2.3. Satellite Data and Climate Indices

2.3.1. Ocean Color and Photosynthetically Active Radiation (PAR)

We used daily and monthly SeaWiFS (1997–2010) and MODIS-Aqua (2002–2015) level-3 $Rrs(\lambda)$ and PAR data with a spatial resolution of 0.083° $\times$ 0.083°, downloaded from NASA's ocean color website (http://oceancolor.gsfc.nasa.gov/). Downloaded $Rrs(\lambda)$ include bands 412, 443, 490, 510, 555, and 670 for SeaWiFS and bands 412, 443, 469, 488, 531, 547, 555, 645, 667, and 678 for MODIS-Aqua. Daily $Rrs(\lambda)$ data were matched to [Chl] measurements for algorithm development, and monthly $Rrs(\lambda)$ data were used to derive NCP time series.

2.3.2. Sea Ice

We estimated sea-ice dynamics from a satellite daily sea-ice concentration data product (1990–2012) which uses a polar stereographic projection with a grid cell size of 25 km $\times$ 25 km (NASA's Scanning Multichannel Microwave Radiometer (SMMR) and the Defense Meteorological Satellite Program's (DMSP) Special Sensor Microwave/Imager (SSM/I); downloaded from the EOS Distributed Active Archive Center (DAAC) at the National Snow and Ice Data Center, University of Colorado in Boulder, Colorado (http://nsidc.org)). From daily sea-ice concentrations, we derived three sea-ice characteristics: day of sea-ice advance, day of sea-ice retreat, and ice-free days. Day of sea-ice advance is defined as the first day when sea-ice concentration is $>$15% for 5 consecutive days. Day of sea-ice retreat is defined as the last day when sea-ice concentration is above 15% for 5 consecutive days, and ice-free days are defined as the number of days with sea-ice concentration $\leq$15% between day of sea-ice retreat and day of sea-ice advance [*Stammerjohn et al*., 2008a].

2.3.3. Wind Speed

Cross-Calibrated Multi-Platform (CCMP) ocean surface wind vectors with a spatial resolution of 0.25° $\times$ 0.25° were downloaded from https://podaac.jpl.nasa.gov/[*Atlas et al*., 2011]. This surface wind product blends data from multiple satellites, providing high temporal resolution (6 h) and a long time series (1987–2011) of wind speed. We used CCMP wind product to examine the relation of sea-ice dynamics to wind speed. We used NCEP Reanalysis wind speed to calculate piston velocities for NCP calculations [*Kalnay et al*., 1996].

2.3.4. Sea Surface Temperature (SST)

Monthly SST was derived from satellite SST acquired by AVHRR (1997–2007) and MODIS-Aqua (2008–2015). AVHRR monthly SST was calculated from daily values with a spatial resolution of 4 km $\times$ 4 km at the equator (http://www.nodc.noaa.gov/SatelliteData/pathfinder4km/). MODIS-Aqua monthly SST with a spatial resolution of 0.083° $\times$ 0.083° was downloaded from NASA's ocean color website (http://oceancolor.gsfc.nasa.gov/).

2.3.5. Climate Indices

Monthly Niño 3.4 indices (as indicators of ENSO activity) were downloaded from https://iridl.ldeo.columbia.edu/. The Niño 3.4 index is calculated from averaged equatorial Pacific SST anomalies in the region between 5°N and 5°S in latitude, and between 170°W and 120°W in longitude [*Cane et al*., 1986]. Monthly SAM index time series were downloaded from http://www.nerc-bas.ac.uk/icd/gjma/sam.html [*Marshall*, 2003]. The SAM index is defined as the difference in zonal mean sea level pressure (SLP) between 40°S and 65°S [*Gong and Wang*, 1999].

2.4. Algorithm Development

2.4.1. Pal-LTER Region-Specific Satellite-[Chl] Algorithm (Pal-[Chl])

As shown by *O'Reilly et al*. [1998], *Kahru and Mitchell* [2010], and *Johnson et al*. [2013], the standard satellite-[Chl] algorithms (OC4v6 and OC3Mv6) underestimate true [Chl] by a factor of two to three in the Southern Ocean. To improve the regional satellite-[Chl] estimation, we developed Pal-LTER region-specific satellite-[Chl] algorithms (Pal-[Chl]) for SeaWiFS (Pal-$[Chl]_s$) and MODIS-Aqua (Pal-$[Chl]_m$).

Our Pal-$[Chl]_s$ and Pal-$[Chl]_m$ have the following form: $log_{10}([Chl])=Slope*log_{10}(MBR)+Intercept$, where MBR stands for maximum band ratio. Considering that match-ups for SeaWiFS and MODIS-Aqua are limited and are of unequal size in each region, we inferred model constants (slope and intercept) using a Bayesian hierarchical model which allows information sharing:

$$log_{10}([Chl])_{i,j,k} \sim Normal\left(\beta_{j,k}log_{10}\left(MBR\right)_{i,j,k}, \delta^2\right) \tag{1}$$

where subscripts i, j, and k represent indices of samples, satellite sensors (SeaWiFS and MODIS-Aqua) and regions, respectively. $\beta_{j,k}$ is a 1×2 vector that consists of model slope and intercept parameters. $log_{10}(MBR)_{i,j,k}$ is a 2×1 vector with the last component equal to 1. Model parameters have the following prior distributions $\beta_{j,k} \sim Normal(\mu, \sum)$, $\mu \sim Normal\left(\mu_0, \sum_0\right)$, $\sum^{-1} \sim Wishart(a^0, b^0)$, and $\delta \sim uniform(0, 100)$, where μ_0, $\sum_0$, a^0 and b^0 are constants. In order for model parameters to be mainly data driven, we used weakly informative priors. The posterior distributions of parameters were approximated using a sequence of random samples simulated through a Markov chain Monte Carlo (MCMC) method. The sequence contains 10,000 iterations to ensure convergence. To eliminate the influence of initial values, the last 5000 samples (burn-in = 5000) were used to summarize posterior distributions.

2.4.2. Derivation of Satellite-NCP Algorithm and Time Series

With all other factors equal, a relation between NCP and [Chl] is to be expected as $NCP=NPP-HR=\mu*[Chl]*\frac{C}{[Chl]}-HR$, where μ and C are phytoplankton growth rate and carbon content, respectively. We tried three independent methods to calculate the relation of NCP to [Chl]. First, following the equation developed by *Huang et al.* [2012], i.e., $log_{10}\ (NCP)=0.79(\pm0.06)log_{10}([Chl])+1.39(\pm0.03),\ \ (n=92, R^2=0.66)$, we derived an updated NCP model based on an ordinary least squares (OLS) regression of in situ [Chl] and historical and new O_2/Ar-NCP estimates (2008–2014). Second, in light of the significant uncertainties in O_2/Ar-NCP estimates in low-value regions [*Jonsson et al.*, 2013], we developed another NCP model using robust Bayesian analysis with e-contaminations (hereafter denoted as e-contamination) [*West*, 1984]. Finally, to take into account the fact that the functional relationship between NCP and [Chl] could vary across regions, we developed an NCP model using a Bayesian hierarchical model:

$$log_{10}(NCP)_{i,k} \sim Normal\left(\beta_k log_{10}([Chl])_{i,k}, \delta^2\right) \tag{2}$$

The format, distributions, parameters, and procedures are similar to the ones for Pal-[Chl].

We derived a time series of satellite MNCP and ANCP for 1997–2014 using the algorithms described above. NCP images were smoothed with a 0.415° × 0.415° window using the criterion that a pixel with >1/3 of its neighbors covered by sea ice or clouds was ignored. ANCP was estimated from austral spring to the subsequent winter with most of the NCP signal observed during the September to April growing season.

2.5. Empirical Orthogonal Function (EOF) Analyses

We decomposed the ANCP time series into spatial (EOFs) and temporal (PC) components through an EOF analysis. Assuming that NCP is lognormally distributed as [Chl] [*Loch*, 1966], we log-transformed ANCP, removed the linear trend by subtracting a linear fit to the ANCP time series from each pixel, and calculated ANCP anomalies by removing the climatology estimated from ANCP in 1997–2014. Finally, we applied an EOF analysis to the time series of ANCP anomalies.

3. Results

3.1. Relationship Between In Situ [Chl] and O_2/Ar-NCP Estimates

NCP predicted by Bayesian hierarchical model is highly correlated to O_2/Ar-NCP estimates ($R^2 = 0.57$, n = 175), with large scatter observed in low-value regions (Figure 2). As determined using the Bayesian hierarchical model, the relationship between NCP and [Chl] varies between regions (Table 1), with steepest and flattest slopes in the offshore regions and middle SZ, respectively. However, the three statistical methods employed (i.e., OLS, e-contamination and Bayesian hierarchical model) result in similar equations. The mean of model coefficients for the Bayesian hierarchical model is close to those of OLS ($log_{10}\ (NCP)=0.80(\pm0.06)\ log_{10}([Chl])+1.36(\pm0.03)$), e-contamination ($log_{10}\ (NCP)=0.75(\pm0.04)log_{10}([Chl])+1.41(\pm0.02)$) and the algorithm developed by *Huang et al.* [2012] ($log_{10}\ (NCP)=0.79(\pm0.06)log_{10}([Chl])+1.39(\pm0.03)$), where the values in the parentheses represent one standard deviation. The consistency between algorithms implies that

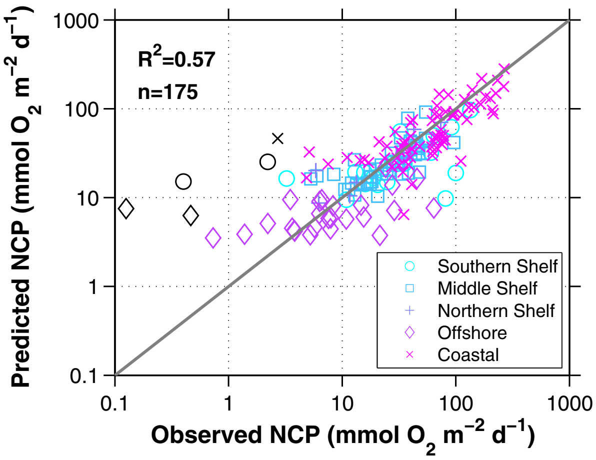

Figure 2. O_2/Ar-NCP measurements and predictions by the Bayesian hierarchical algorithm. "Coastal" represents region ≤50 km from the coast. Axes are logarithmic.

the functional relationship between in situ [Chl] and O_2/Ar-NCP estimates is robust and stable over multiple years. Although the Bayesian hierarchical model captures part of the regional variations in the relationship between NCP and [Chl], estimating NCP using subregion algorithms does not significantly improve predictions, indicating that parameters other than [Chl] also control NCP variability or that uncertainties in in situ observations preclude further improvements. As such, for simplicity we derived the satellite time series of NCP using the mean coefficients from the Bayesian hierarchical model.

To assess which variables are the best predictors of NCP, we also conducted a variable selection analysis using a stochastic search variable selection (SSVS) [*George and Mcculloch*, 1993] with the following in situ variables: [Chl], [POC], sea surface salinity (SSS), mixed layer depth (MLD), PAR, and SST. We found that NCP is best predicted by [POC] and SSS, followed by [Chl]. *Cassar et al*. [2015] recently highlighted a strong relationship between NCP and [POC] in the Australian sector of the Southern Ocean. In the supporting information, we present a satellite-[POC] algorithm specific to the Pal-LTER region. We opt to use Pal-[Chl] instead of [POC] algorithms for NCP reconstruction because satellite estimates of [Chl] are more accurate than [POC].

3.2. Pal-LTER Region-Specific Satellite-[Chl] Algorithm (Pal-[Chl])

Our satellite-[Chl] algorithms (Table 1) predict [Chl] relatively well and are arguably comparable or better than the standard satellite-[Chl] algorithms (OC4v6 and OC3Mv6), and other Southern Ocean algorithms [*Dierssen and Smith*, 2000; *Johnson et al*., 2013] (Figure 3). The underestimation of [Chl] in the Southern Ocean by OC4v6 and OC3Mv6 is rectified by the other algorithms to various degrees. However, uncertainties remain significant especially for higher values, which are mainly observed in the coastal region where other optically active components may not covary with [Chl] (i.e., Case 2 waters) [*Morel and Prieur*, 1977]. Although differences in the model coefficients for each region are observed (Table 1), subregion models do not significantly improve [Chl] estimates. Therefore, for simplicity we used mean model coefficients to derive our [Chl] time series. We note that the algorithm of *Dierssen and Smith* [2000] was tuned using in situ *Rrs*(λ) which have lower uncertainties than satellite data. Although their algorithm was developed for SeaWiFS, it performs well when applied to MODIS-Aqua.

Table 1. Coefficients of NCP and Satellite-[Chl] Algorithms for Individual Regions[a]

Algorithm Coefficients	Southern Shelf	Middle Shelf	Northern Shelf	Offshore	Coastal	Mean
NCP						
Slope	0.73 (0.14)	0.69 (0.13)	0.73 (0.16)	0.84 (0.15)	0.71 (0.09)	0.75 (0.14)
Intercept	1.29 (0.08)	1.42 (0.05)	1.26 (0.11)	1.29 (0.09)	1.43 (0.05)	1.33 (0.10)
Pal-$[Chl]_s$						
Slope	−2.62 (0.66)	−2.41 (0.30)	−2.74 (0.47)	−2.49 (0.34)	−2.53 (0.29)	−2.62 (0.28)
Intercept	0.74 (0.24)	0.66 (0.10)	0.75 (0.17)	0.62 (0.13)	0.75 (0.10)	0.76 (0.10)
Pal-$[Chl]_m$						
Slope	−1.95 (0.25)	−2.26 (0.33)	−1.95 (0.48)	−2.08 (0.33)	−1.76 (0.26)	−1.95 (0.21)
Intercept	0.33 (0.10)	0.43 (0.06)	0.30 (0.18)	0.29 (0.11)	0.36 (0.09)	0.30 (0.06)

[a]The NCP algorithms have the form: $log_{10}(NCP)=\text{Slope}*log_{10}([Chl])+\text{Intercept}$. Satellite-[Chl] algorithms have the form: $log_{10}([Chl])=\text{Slope}*log_{10}(MBR)+\text{Intercept}$, where $MBR=\max\left\{\frac{Rrs(443)}{Rrs(555)},\frac{Rrs(490)}{Rrs(555)},\frac{Rrs(510)}{Rrs(555)}\right\}$ for SeaWiFS and $MBR=\max\left\{\frac{Rrs(443)}{Rrs(547)},\frac{Rrs(488)}{Rrs(547)}\right\}$ for MODIS-Aqua. "Offshore" represents POOZ and SACCF regions. "Coastal" denotes coastal region (≤50 km from coast). "Mean" represents the mean of coefficients for five regions. Values in parentheses represent one standard deviation.

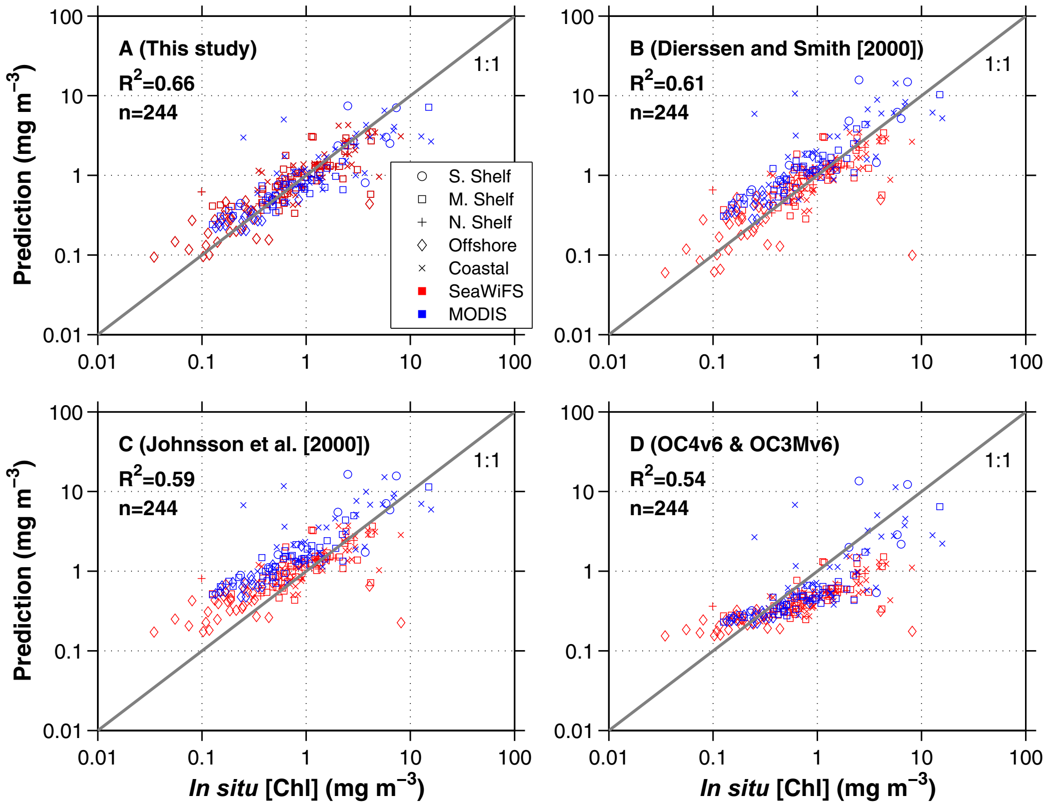

Figure 3. Comparison of in situ [Chl] to satellite (SeaWiFS and MODIS-Aqua) predictions based on (a) algorithms developed in this study, (b) *Dierssen and Smith* [2000]; (c) *Johnson et al.* [2013]; and (d) global standard satellite-[Chl] algorithms of OC4v6 and OC3Mv6. Axes are logarithmic.

3.3. NCP Reconstruction From Satellite Data

3.3.1. NCP Climatology

High NCP generally proceeds from offshore to onshore regions roughly following the climatology of sea-ice retreat (Figure 4). In the POOZ, NCP is generally low during the entire growing season potentially due to deep mixed layers and/or low iron availability. In the SACCFZ, NCP is high during sea-ice retreat between October and December and becomes low thereafter. In the SZ, NCP peaks in December-January, and remains high thereafter. SZ also displays higher NCP in the austral summer than offshore regions (POOZ and SACCFZ). In the austral summer after sea-ice retreat, a north-south gradient in NCP is observed in the SZ, with high values in the southern portion of the WAP (e.g., Marguerite Bay and Marguerite Trough).

Overall, we find that the SZ and more specifically regions associated with submarine canyons (e.g., Marguerite Trough) are up to 8 times more productive than the offshore regions (POOZ and SACCFZ) (Figure 5). The longer growing season and difference in NCP phenology in the north likely explain the weaker north-south gradient in the ANCP compared to the MNCP climatology. NCP for each month are presented in the supporting information.

3.3.2. NCP Spatiotemporal Variability

The first EOF mode explains ~50% of ANCP variance and shows large regional differences (Figure 6a). We will only analyze the first PC and EOF hereafter. High values in the EOF represent high interannual variability (IAV), such as in the southern and middle SACCFZ. Conversely, low values in the EOF represent low IAV, such as in the POOZ. In the SZ, the IAV of ANCP is heterogeneous, with high values around the head of Marguerite Trough and low values in the north and in Ryder Bay. For simplicity, we hereafter define the high IAV region (contoured area in Figure 6a) as a high temporal variability (HTV) region, roughly bounded by the climatology of the Southern Antarctic Circumpolar Current Front (as defined by *Orsi et al.* [1995]) (Figure 1). We note that our estimates of IAV are normalized to the climatology (see section 2.5).

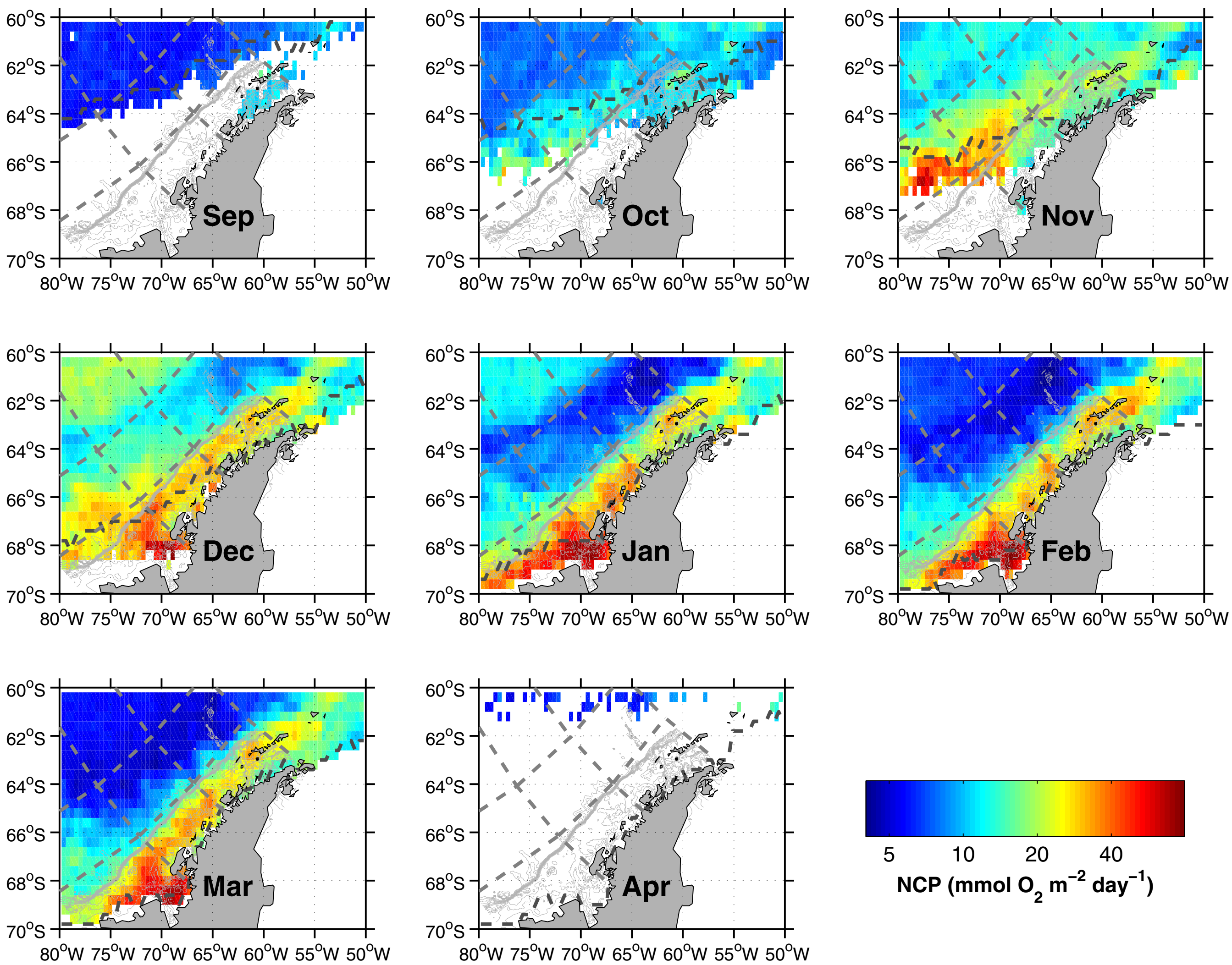

Figure 4. Climatology of MNCP derived from 1997 to 2014 time series. Thin gray lines represent 250 m-increment isobaths, which collapse into a thick gray line at the shelf break. Thick black-dashed line is the climatology of the ice edge for that month from 1990 to 2012. Gray dashed line separates the WAP region into nine subregions as defined in Figure 1. White area is covered by sea ice/cloud. NCP is on a logarithmic scale.

The first PC of ANCP varies, with low values in 1997 and 2002 and high values in 2005 and 2006 (Figure 6b). High values in the PC correspond to high ANCP in the HTV region (and vice versa). Large phytoplankton blooms are observed from November to January in 2005 and 2006, whereas there are no blooms for the whole growing season in 2002 in the HTV region (see supporting information). To find the potential drivers of ANCP IAV, we compared the first PC with the SAM and Niño 3.4 climate indices and found significant correlations in particular months and seasons (Table 2). For example, we found that in austral spring the first PC is negatively correlated to the Niño 3.4 climate index and positively correlated to the SAM climate index (Table 2 and Figure 7). The first PC shows the highest correlation with average SAM in October and November ($R = 0.7$, $p < 0.01$). This time window (October and November) includes the date of sea-ice retreat in the HTV region (Figure 4). Following these results, we compared MNCP in each subregion during years with positive and negative average SAM in October and November. We found that, in the SZ and SACCFZ, NCP is generally higher in positive SAM years than negative SAM years (Figure 8), with the largest difference observed in the southern and middle SACCFZ. Maintaining the time series will be important to assess whether these results are significant.

We also conducted an EOF analysis of annually averaged NCP (as opposed to annually integrated NCP) to account for the effect of changes in number of ice-free days. For example, 1 year's average NCP may be very low, but integrated NCP high if the number of ice-free days is long. Annually averaged NCP shows

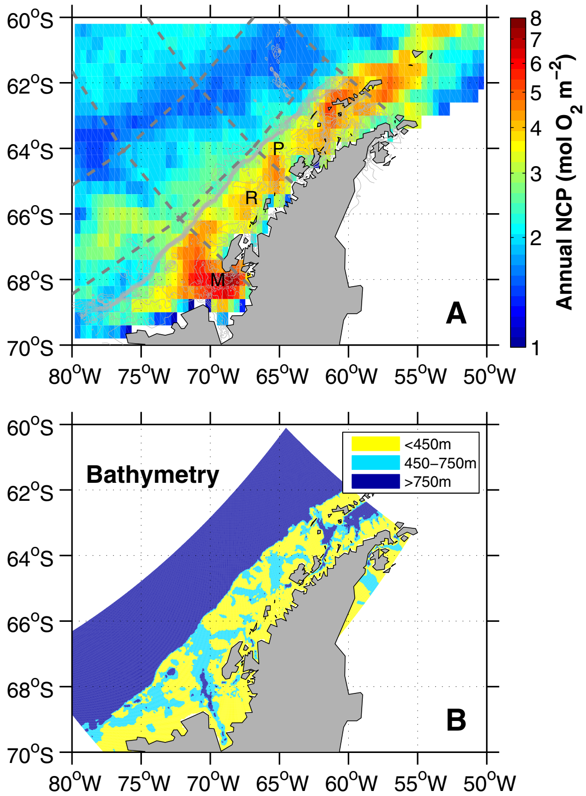

Figure 5. (a) Climatology of ANCP calculated from 1997 to 2014 time series and (b) color-coded bathymetry for the WAP region. Thin gray lines represent 250 m-increment isobaths, which collapse into a thick gray line at the shelf break. Gray dashed line separates the WAP region into nine subregions as defined in Figure 1. Letters P, R, and M identify Palmer deep, Renaud canyon, and Marguerite Trough, respectively. White area is covered by sea ice/cloud. NCP is on a logarithmic scale.

similar EOF and PC patterns to those shown by ANCP (Figure 6). EOF analysis of summer-integrated NCP also yielded similar results (see supporting information).

4. Discussion

4.1. NCP Estimation

The uncertainties in our satellite-NCP estimates mainly originate from the regression between in situ O_2/Ar-NCP estimates and [Chl], as well as the uncertainties in satellite-[Chl] estimates. The regression between O_2/Ar-NCP estimates and [Chl] is based on the assumption that NCP solely depends on [Chl] and that this dependence does not vary in time or space. However, NCP is also associated with other factors such as SST, phytoplankton physiological status, and community structure [*Boyd and Trull*, 2007; *Huang et al.*, 2012; *Laws et al.*, 2000; *Rivkin and Legendre*, 2001]. There are also uncertainties associated with O_2/Ar-NCP estimates (e.g., steady state assumption, and gas exchange parameterization) [see *Bender et al.*, 2011; *Cassar et al.*, 2014; *Jonsson et al.*, 2013]. For example, the assumption of steady state may be violated during vigorous blooms in the early growing season (Figure 2). Previous studies also observed strong seasonality in the NCP [*Bushinsky and Emerson*, 2015; *Emerson*, 2014; *Fassbender et al.*, 2016; *Ostle et al.*, 2015; *Palevsky et al.*, 2016]. Net heterotrophy and entrainment of newly exported production back into the mixed layer, more commonly observed in the fall and winter [*Bushinsky and Emerson*, 2015; *Emerson*, 2014; *Fassbender et al.*, 2016; *Kortzinger et al.*, 2008; *Ostle et al.*, 2015; *Palevsky et al.*, 2016], are not captured by our current algorithms. Therefore, our ANCP is different from the one presented in previous studies [*Bushinsky and Emerson*, 2015; *Emerson*, 2014; *Palevsky et al.*, 2016] and may overestimate NCP in the late part of growing season (i.e., austral autumn).

Although regional algorithms developed in this study and by *Dierssen and Smith* [2000] can predict [Chl] relatively well, large scatter is observed and significantly limits the accuracy of our satellite-NCP estimates. Our satellite-[Chl] algorithms were calibrated using in situ [Chl] mostly obtained from the shelf and coastal

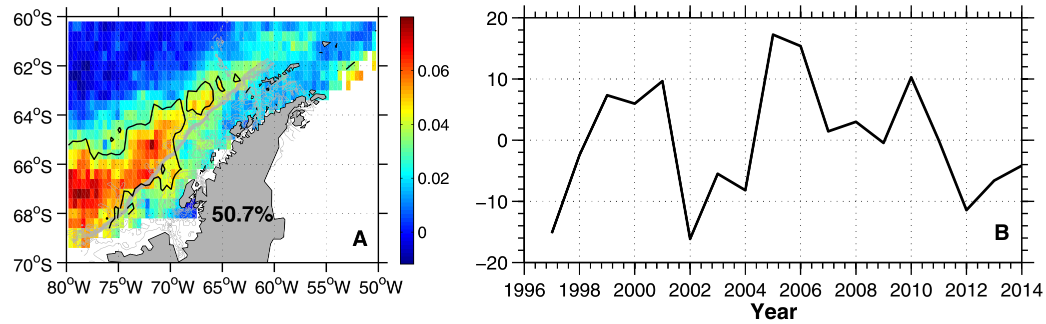

Figure 6. (a) The first EOF and (b) PC for ANCP. The high temporal variability (HTV) region is contoured in black.

Table 2. Correlation Coefficients Between the First PC of ANCP and SAM and ENSO Climate Indices[a]

Climate Index Month/Season	First PC Versus Niño 3.4	First PC Versus SAM
6	−0.46	0.10
7	**−0.51**	−0.15
8	**−0.55**	−0.23
9	**−0.54**	0.14
10	**−0.50**	***0.65***
11	**−0.52**	**0.48**
12	**−0.49**	0.00
13	**−0.49**	0.04
14	**−0.48**	0.00
15	**−0.56**	−0.28
16	−0.46	−0.41
17	−0.30	−0.06
6–8(Winter)	**−0.52**	−0.15
9–11(Spring)	**−0.52**	***0.63***
12–14(Summer)	**−0.49**	0.01
15–17(Autumn)	**−0.49**	−0.46

[a]The first column shows the month/austral season of climate indices for the correlation analyses, with numbers >12 representing months in the subsequent year. Correlations that exceed the 0.05 and 0.01 significance levels are in bold and italicized bold, respectively.

regions. More in situ [Chl] measurements are required to validate the transferability of our regression to the offshore regions. In addition, our in situ O_2/Ar-NCP estimates and satellite measurements are only relevant to the mixed layer and first optical depth, respectively, missing production below the mixed layer (e.g., deep chlorophyll maximum) and under sea ice [*Korb et al*., 2004; *Moline and Prezelin*, 2000].

4.2. NCP Biogeography

In the WAP region, phytoplankton growth rate is thought to be largely controlled by iron [*Garibotti et al*., 2005, 2003; *Huang et al*., 2012; *Martin and Gordon*, 1988; *Martin et al*., 1990], light availability [*Mitchell et al*., 1991; *Nelson and Smith*, 1991], and/or grazing [*Ainley et al*., 2007; *Bernard et al*., 2012; *Frost*, 1991; *Frost and Franzen*, 1992; *Garzio et al*., 2013; *Holm-Hansen and Huntley*, 1984]. The iron sources in this region are mainly from sea-ice meltwater [*Lannuzel et al*., 2007, 2008], glacial discharges [*Dierssen et al*., 2002], and/or vertical mixing of subsurface waters [*Ducklow et al*., 2007; *Martinson et al*., 2008; *Tagliabue et al*., 2014]. The light regime is also affected by sea-ice dynamics, glacial melt, and melt-freeze changes in water column stratification [*Mitchell and Holm-Hansen*, 1991; *Saba et al*., 2014; *Smith and Nelson*, 1986; *Venables et al*., 2013]. For example, *Saba et al*. [2014] and *Venables et al*. [2013] found that later sea-ice retreat is associated with higher in situ [Chl] in January in the SZ. They hypothesized that later sea-ice retreat shields the water column from wind mixing, and that the meltwater stratifies the water column therefore allowing phytoplankton to remain in the upper water column under favorable light conditions.

Huang et al. [2012] found that F_v/F_m measurements reveal a negative onshore-to-offshore gradient, indicating that iron availability decreases with distance from shore. This onshore-to-offshore decline pattern in dissolved iron largely controls the spatial pattern of our ANCP. The timing of our peak in NCP generally follows ice edge, suggesting an influence of sea-ice meltwater on light and/or iron availability.

Submarine canyons are hypothesized to steer iron-rich and warm Upper Circumpolar Deep Water (UCDW) into the shelf and coastal regions [*Schofield et al*., 2013]. We found that NCP is generally higher in some submarine canyon regions than in the adjacent regions (Figures 4 and 5). Our result is consistent with that of *Kavanaugh et al*. [2015] who compared biological and physical parameters above and adjacent to canyons.

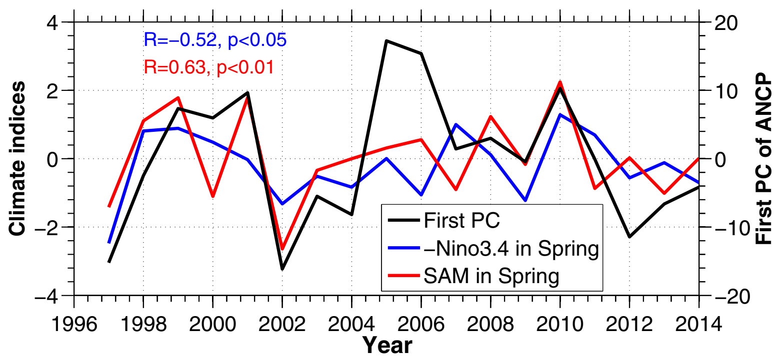

Figure 7. Correlation between the first PC of ANCP and the SAM and Niño 3.4 climate indices in austral spring. Note the reverse Niño 3.4 scale.

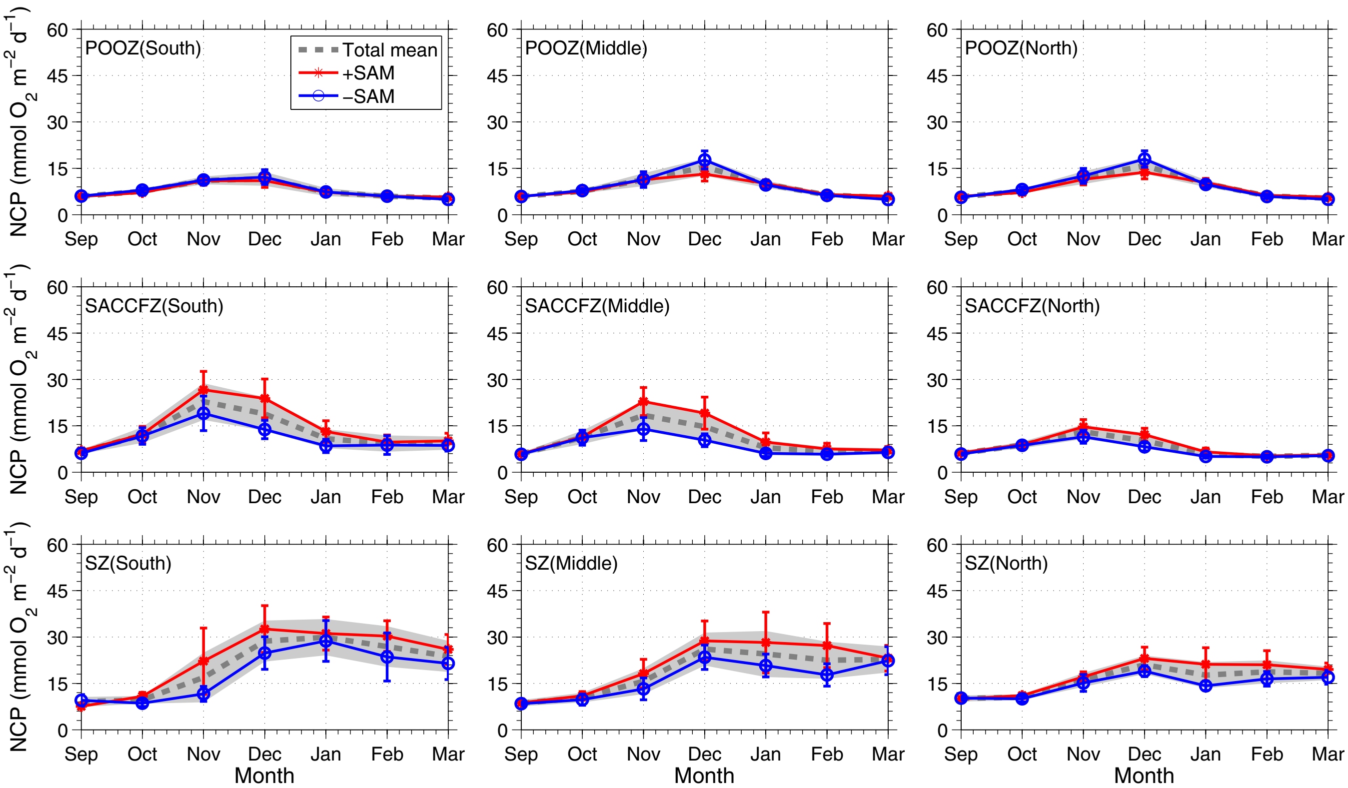

Figure 8. Multiyear arithmetic mean of MNCP in each subregion for the years with positive (1998, 1999, 2001, 2005, 2006, 2008, 2009, 2010, and 2014, red line) and negative SAM (1997, 2000, 2002, 2003, 2004, 2007, 2011, 2012, and 2013, blue line). MNCP is calculated as the geometric average of grids in each subregion. Dashed-gray line represents the climatological seasonal cycle for 1997–2014. Shaded area and the length of vertical lines represent one standard deviation.

Our algorithm also predicts enhanced NCP around the submarine canyon next to Renaud Island where an Adélie penguin colony is observed. We note that NCP patterns do not exactly match the canyons in some regions, likely because of the influence of other factors such as lateral advection. A more careful examination of the role of canyons in fueling NCP hotspots will be the subject of a future study.

4.3. NCP Interannual Variability and Climate Indices

ANCP in the WAP region is believed to be controlled in large part by sea-ice dynamics which in turn are conditioned by large-scale atmospheric circulation [*Stammerjohn et al.*, 2008a]. In order to study the effect of large-scale forcings on ANCP, we first examined the association of sea-ice dynamics to the SAM and Niño 3.4 climate indices and then explored the IAV in sea-ice dynamics and ANCP.

4.3.1. Climate Indices and Sea Ice

Our updated results support previous studies [*Massom et al.*, 2006; *Stammerjohn et al.*, 2008a] that stronger northerly winds result in an earlier sea-ice retreat and a later sea-ice advance (Table 3). Positive phases in SAM or negative phases in ENSO are associated with low SLP around the Amundsen Sea and intensified northerly winds that transport heat and momentum to the WAP region, leading to an earlier sea-ice retreat and a later sea-ice advance [*Massom et al.*, 2006; *Stammerjohn et al.*, 2008a].

4.3.2. NCP Interannual Variability

Over the timescale of our study, we do not observe a long-term trend in sea ice or ANCP. Our results are however consistent with sea ice governing interannual variability and seasonality of NCP in the WAP region [*Ross et al.*, 2008; *Smith et al.*, 1995, 2008; *Vernet et al.*, 2008]. We also find a statistically significant trend of decreasing austral spring-averaged NCP in all subregions, except the southern sector of the SZ (Figure 9). In the HTV region, higher ANCP is observed in years with higher SST ($R = 0.66$, $p < 0.01$), longer growing seasons ($R = 0.49$, $p = 0.06$), and an earlier sea-ice retreat ($R = -0.58$, $p < 0.05$). Similar results for annually integrated NPP in the WAP have recently been reported by *Moreau et al.* [2015]. Years with more ice-free days and higher ANCP display higher midsummer NCP (e.g., 2005 and 2006) (Figure 10), suggesting that other

Table 3. Correlation Between Climate Indices, Wind Speed, and Sea-Ice Dynamics in Each Subregion[a]

	Niño 3.4		SAM		Wind Speed	
Subregion	Retreat	Advance	Retreat	Advance	Retreat	Advance
POOZ						
North						
Middle	0.25	**−0.44**	−0.28	**0.45**	**0.53**	***−0.71***
South	***0.56***	**−0.44**	−0.39	0.35	***0.67***	**−0.64**
SACCFZ						
North	0.36	**−0.44**	−0.27	0.41	0.50	***−0.85***
Middle	***0.62***	**−0.43**	**−0.44**	**0.43**	***0.70***	***−0.78***
South	0.40	**−0.43**	−0.37	0.36	***0.78***	−0.32 (**−0.54**)
SZ						
North	0.36	−0.36	−0.33	**0.44**	**0.56**	**−0.58**
Middle	**0.51**	***−0.61***	−0.27	0.18	**0.53**	−0.38 (***−0.67***)
South	0.35	***−0.69***	**−0.46**	0.04	***0.76***	0.04 (**−0.56**)

[a]Correlations that exceed the 0.05 and 0.01 significance levels are in bold and italicized bold, respectively. Only the meridional component of wind speed is presented (northward is positive). Day of sea-ice retreat was compared to averaged climate indices/wind speed in austral spring (September–November). Day of sea-ice advance was compared to averaged climate indices/wind speed in austral winter (June–August), with values in parentheses representing correlation in austral autumn (March–May). We show these additional correlations because sea ice advances in austral autumn in these regions [*Stammerjohn et al.*, 2008a]. The northern sector of POOZ was not covered by sea ice every year, and thus the correlation is not presented.

factors (e.g., iron and light) preconditioned by or associated with the length of the growing season have ramifications throughout the growing season.

In order to explore this further, we look at IAV in the light regime in the HTV region. Like *Tortell et al*. [2014] who used in situ observations, we found an association between NCP and surface PAR in the HTV region in the austral summer ($R = 0.59$, $p < 0.01$; see supporting information figure). Unfortunately, we do not have a good proxy for IAV in MLD which is likely a more dominant control on light availability.

Similarly, we do not have IAV in iron observations and can only speculate on how iron availability may be impacted by the number of ice-free days. As atmospheric deposition is limited in the HTV region [*Cassar*

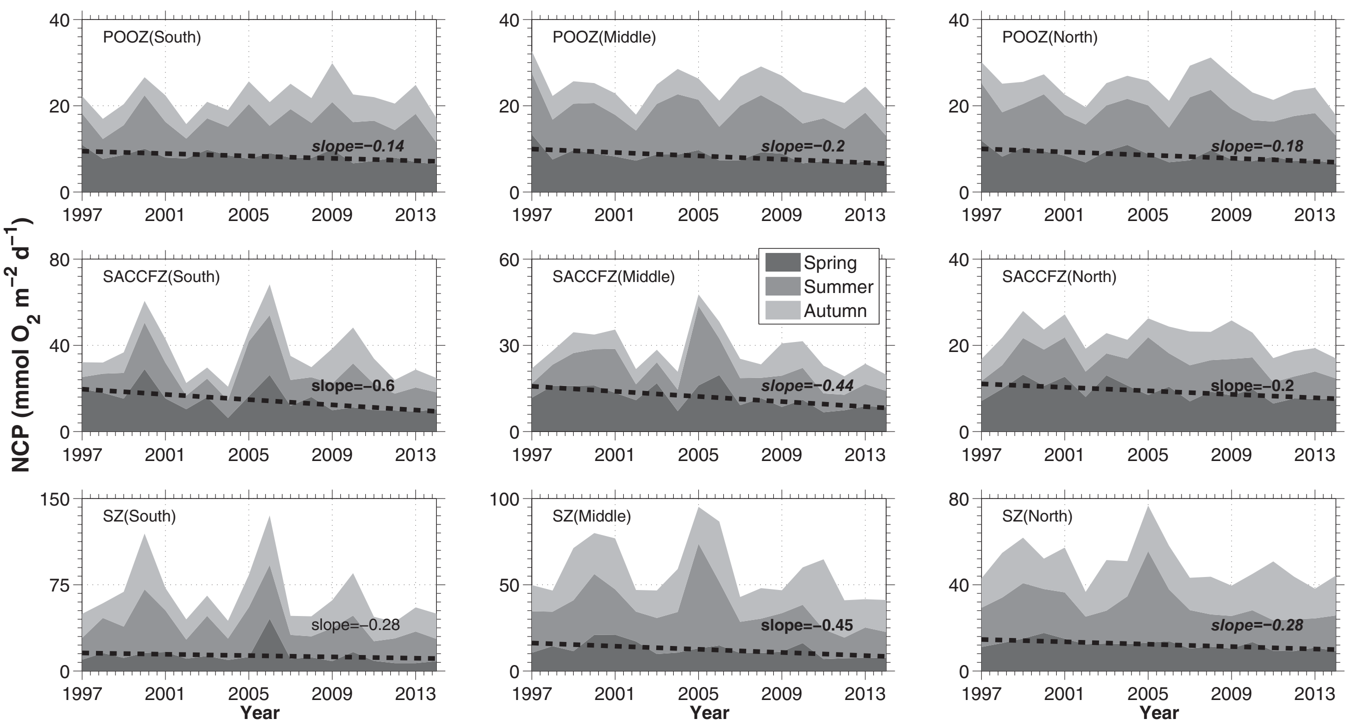

Figure 9. Trends of spring-averaged (September–November) NCP in individual subregions. Black-dashed lines represent the trends, with trends that exceed the 0.05 and 0.01 significance levels shown in bold and italicized bold, respectively. Note that *y* axes have different ranges.

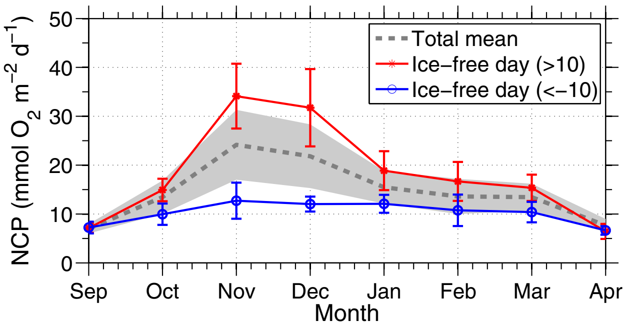

Figure 10. Multiyear arithmetic mean of MNCP in the high temporal variability (HTV) region for years with ice-free days $>$10 days average (1999, 2005, 2006, 2007, 2008, and 2010, red line) and <-10 days average (2001, 2002, 2003, 2004, and 2012, blue line). Dashed-gray line represents climatology for 1997–2014. Shaded area and the length of vertical lines represent one standard deviation.

et al., 2007], the main iron sources are likely from ice melt and obduction of subsurface iron-rich waters. In the Weddell Sea, studies have found that weakening winds can shift the boundary current toward shore, increasing the interaction between offshore waters and the shelf [*Thompson and Youngs*, 2013; *Youngs et al*., 2015]. In the WAP region, IAV in northerly wind strength could influence the extent of interactions of the boundary current with iron-rich shelf waters. We hypothesize that years with stronger winds and lower sea ice extent could lead to increased winter mixing and availability of iron in the HTV region [*Sokolov and Rintoul*, 2007; *Venables et al*., 2013], and/or directly through lateral advection [*Graham et al*., 2015; *Sokolov and Rintoul*, 2007]. However, more observations will be required to assess the influence of sea-ice dynamics on iron supply and NCP in the WAP.

5. Summary and Conclusions

In this study, we used satellite data to examine interannual variability of NCP at the WAP. We derived a time series of NCP (1997–2014) using newly developed regional satellite-[Chl] algorithms and an updated regression between in situ [Chl] and O_2/Ar-NCP estimates. We find higher annually integrated NCP in the SZ, especially in submarine canyon regions (e.g., Marguerite Trough). NCP generally peaks around January/November–December in the SZ/southern and middle SACCFZ, while NCP and its seasonal and interannual variability are low in the POOZ. Annually integrated NCP in the southern and middle SACCFZ shows the highest interannual variability, which is associated with sea-ice dynamics, SST, PAR, and the ENSO and SAM climate indices.

The SAM index has intensified over the last 40 years. This trend is predicted to persist in the future [*Marshall*, 2003; *Thompson et al*., 2000], resulting in an earlier sea-ice retreat [*Stammerjohn et al*., 2008a, 2008b] and enhanced NCP and surface biological carbon export. Although we do not observe a trend in annually integrated NCP, we find a decreasing trend in austral spring-averaged NCP in all the subregions excluding the southern sector of the SZ. Changes in the seasonality of NCP may have a large impact on higher trophic-level organisms such as penguins which breed during specific seasons. It will be important to monitor future changes in the region's biological pump and its seasonality with the predicted strengthening of the SAM.

Appendix A: List of Acronyms and Abbreviations

Acronyms	Description
[Chl]	Chlorophyll a concentration
[POC]	Particulate organic carbon concentration
ANCP	Annually integrated net community production
Ar	Argon
ENSO	El Niño Southern Oscillation
EOF	Empirical Orthogonal Function
HR	Heterotrophic respiration
HTV	High temporal variability
IAV	Interannual variability
MBR	Maximum band ratio
MCMC	Markov chain Monte Carlo
MLD	Mixed layer depth
MNCP	Monthly net community production

NCP	Net community production
NPP	Net primary production
O_2	Oxygen
OLS	Ordinary least squares
Pal-[Chl]	Pal-LTER region-specific satellite-[Chl] algorithm
Pal-$[Chl]_m$	Pal-[Chl] for MODIS-Aqua data
Pal-$[Chl]_s$	Pal-[Chl] for SeaWiFS data
PAR	Photosynthetically active radiation
PC	Principle component
POOZ	Permanently open ocean zone
$Rrs(\lambda)$	Remote sensing reflectance just above water surface
SACCFZ	Southern Antarctic Circumpolar Current Front Zone
SAM	Southern Annual Mode
SLP	Sea level pressure
SSS	Sea surface salinity
SST	Sea surface temperature
SSVS	Stochastic search variable selection
SZ	Shelf zone
UCDW	Upper Circumpolar Deep Water
WAP	Western Antarctic Peninsula
μ	Phytoplankton growth rate
C	Phytoplankton carbon content

Acknowledgments
This study was supported by a NASA Earth and Space Science Fellowship (NNX13AN85H) to Z.L. and an NSF (OPP-1043339) grant to N.C. In situ data collection was supported by NSF awards OPP-9632763 to R.C. Smith (University of California at Santa Barbara) and 0217282, 0823101, and 1440435 to H. Ducklow. The authors acknowledge NASA GSFC SeaWiFS and MODIS-Aqua data products. The authors also thank S. Wang (Duke) and two anonymous reviewers whose valuable comments have greatly improved the manuscript. In situ measurements were downloaded from http://pal.lternet.edu/. Ocean-color data were downloaded from http://oceancolor.gsfc.nasa.gov/. The 1997–2012 SMMR-SSM/I sea-ice concentration data set was downloaded from EOS Distributed Active Archive Center (DAAC) at the National Snow and Ice Data Center, University of Colorado in Boulder, Colorado (http://nsidc.org). Cross-Calibrated Multi-Platform (CCMP) ocean surface wind vectors were downloaded from https://podaac.jpl.nasa.gov/. AVHRR SST was downloaded from http://www.nodc.noaa.gov/SatelliteData/pathfinder4km/. Monthly Niño 3.4 and SAM indices were downloaded from https://iridl.ldeo.columbia.edu/and http://www.nerc-bas.ac.uk/icd/gjma/sam.html, respectively.

References

Ainley, D., et al. (2007), Paradigm lost, or is top-down forcing no longer significant in the Antarctic marine ecosystem?, *Antarct. Sci.*, *19*(3), 283–290.

Atlas, R., R. N. Hoffman, J. Ardizzone, S. M. Leidner, J. C. Jusem, D. K. Smith, and D. Gombos (2011), A cross-calibrated, multiplatform ocean surface wind velocity product for meteorological and oceanographic applications, *Bull. Am. Meteorol. Soc.*, *92*(2), 157–174.

Bender, M. L., S. Kinter, N. Cassar, and R. Wanninkhof (2011), Evaluating gas transfer velocity parameterizations using upper ocean radon distributions, *J. Geophys. Res.*, *116*(C2), C02010, doi:10.1029/2009JC005805.

Bernard, K. S., D. K. Steinberg, and O. M. E. Schofield (2012), Summertime grazing impact of the dominant macrozooplankton off the Western Antarctic Peninsula, *Deep Sea Res., Part I*, *62*, 111–122.

Boyd, P. W., and T. W. Trull (2007), Understanding the export of biogenic particles in oceanic waters: Is there consensus?, *Prog. Oceanogr.*, *72*(4), 276–312.

Brix, H., N. Gruber, D. M. Karl, and N. R. Bates (2006), On the relationships between primary, net community, and export production in subtropical gyres, *Deep Sea Res., Part II*, *53*(5–7), 698–717.

Buesseler, K. O., A. M. P. McDonnell, O. M. E. Schofield, D. K. Steinberg, and H. W. Ducklow (2010), High particle export over the continental shelf of the west Antarctic Peninsula, *Geophys. Res. Lett.*, *37*(22), L22606, doi:10.1029/2010GL045448.

Bushinsky, S., and S. Emerson (2015), Marine biological production from in situ oxygen measurements on a profiling float in the subarctic Pacific Ocean, *Global Biogeochem. Cycles*, *29*, 2050–2060, doi:10.1002/2015GB005251.

Cane, M. A., S. E. Zebiak, and S. C. Dolan (1986), Experimental forecasts of El-Niño, *Nature*, *321*(6073), 827–832.

Cassar, N., M. L. Bender, B. A. Barnett, S. Fan, W. J. Moxim, H. Levy, and B. Tilbrook (2007), The Southern Ocean biological response to aeolian iron deposition, *Science*, *317*(5841), 1067–1070.

Cassar, N., P. J. DiFiore, B. A. Barnett, M. L. Bender, A. R. Bowie, B. Tilbrook, K. Petrou, K. J. Westwood, S. W. Wright, and D. Lefevre (2011), The influence of iron and light on net community production in the Subantarctic and Polar Frontal Zones, *Biogeosciences*, *8*(2), 227–237.

Cassar, N., C. D. Nevison, and M. Manizza (2014), Correcting oceanic O_2/Ar-net community production estimates for vertical mixing using N_2O observations, *Geophys. Res. Lett.*, *41*, 8961–8970, doi:10.1002/2014GL062040.

Cassar, N., S. W. Wright, P. G. Thomson, T. W. Trull, K. J. Westwood, M. de Salas, A. Davidson, I. Pearce, D. M. Davies, and R. J. Matear (2015), The relation of mixed-layer net community production to phytoplankton community composition in the Southern Ocean, *Global Biogeochem. Cycles*, *29*, 446–462, doi:10.1002/2014GB004936.

Chang, C. H., N. C. Johnson, and N. Cassar (2014), Neural network-based estimates of Southern Ocean net community production from *in situ* O_2/Ar and satellite observation: A methodological study, *Biogeosciences*, *11*(12), 3279–3297.

Clarke, A., E. J. Murphy, M. P. Meredith, J. C. King, L. S. Peck, D. K. A. Barnes, and R. C. Smith (2007), Climate change and the marine ecosystem of the Western Antarctic Peninsula, *Philos. Trans. R. Soc. B*, *362*(1477), 149–166.

Craig, H., and T. Hayward (1987), Oxygen supersaturation in the ocean: Biological versus physical contributions, *Science*, *235*(4785), 199–202.

Dierssen, H. M., and R. C. Smith (2000), Bio-optical properties and remote sensing ocean color algorithms for Antarctic Peninsula waters, *J. Geophys. Res.*, *105*(C11), 26,301–26,312.

Dierssen, H. M., R. C. Smith, and M. Vernet (2002), Glacial meltwater dynamics in coastal waters west of the Antarctic peninsula, *Proc. Natl. Acad. Sci. U. S. A.*, *99*(4), 1790–1795.

Ducklow, H. W., W. Fraser, D. M. Karl, L. B. Quetin, R. M. Ross, R. C. Smith, S. E. Stammerjohn, M. Vernet, and R. M. Daniels (2006), Water-column processes in the West Antarctic Peninsula and the Ross Sea: Interannual variations and foodweb structure, *Deep Sea Res., Part II*, *53*(8–10), 834–852.

Ducklow, H. W., K. Baker, D. G. Martinson, L. B. Quetin, R. M. Ross, R. C. Smith, S. E. Stammerjohn, M. Vernet, and W. Fraser (2007), Marine pelagic ecosystems: The West Antarctic Peninsula, *Philos. Trans. R. Soc. B*, *362*(1477), 67–94.

Ducklow, H. W., M. Erickson, J. Kelly, M. Montes-Hugo, C. A. Ribic, R. C. Smith, S. E. Stammerjohn, and D. M. Karl (2008), Particle export from the upper ocean over the continental shelf of the west Antarctic Peninsula: A long-term record, 1992–2007, *Deep Sea Res., Part II*, *55*(18–19), 2118–2131.

Emerson, S. (2014), Annual net community production and the biological carbon flux in the ocean, *Global Biogeochem. Cycles*, *28*, 14–28, doi:10.1002/2013GB004680.

Eppley, R. W., and B. J. Peterson (1979), Particulate organic matter flux and planktonic new production in the deep ocean, *Nature*, *282*, 677–680.

Fassbender, A. J., C. Sabine, and M. F. Cronin (2016), Net community production and calcification from 7 years of NOAA Station Papa Mooring measurements, *Global Biogeochem. Cycles*, *30*, 250–267, doi:10.1002/2015GB005205.

Frost, B. W. (1991), The role of grazing in nutrient-rich areas of the open sea, *Limnol. Oceanogr.*, *36*(8), 1616–1630.

Frost, B. W., and N. C. Franzen (1992), Grazing and iron limitation in the control of phytoplankton stock and nutrient concentration: A chemostat analog of the Pacific equatorial upwelling zone, *Mar. Ecol. Prog. Ser.*, *83*(2–3), 291–303.

Garibotti, I. A., M. Vernet, M. E. Ferrario, R. C. Smith, R. M. Ross, and L. B. Quetin (2003), Phytoplankton spatial distribution patterns along the Western Antarctic Peninsula (Southern Ocean), *Mar. Ecol. Prog. Ser.*, *261*, 21–39.

Garibotti, I. A., M. Vernet, R. C. Smith, and M. E. Ferrario (2005), Interannual variability in the distribution of the phytoplankton standing stock across the seasonal sea-ice zone west of the Antarctic Peninsula, *J. Plankton Res.*, *27*(8), 825–843.

Garzio, L. M., D. K. Steinberg, M. Erickson, and H. W. Ducklow (2013), Microzooplankton grazing along the Western Antarctic Peninsula, *Aquat. Microbial Ecol.*, *70*(3), 215–232.

George, E. I., and R. E. Mcculloch (1993), Variable selection via Gibbs sampling, *J. Am. Stat. Assoc.*, *88*(423), 881–889.

Gong, D. Y., and S. W. Wang (1999), Definition of Antarctic Oscillation index, *Geophys. Res. Lett.*, *26*(4), 459–462.

Graham, R. M., A. M. De Boer, E. van Sebille, K. E. Kohfeld, and C. Schlosser (2015), Inferring source regions and supply mechanisms of iron in the Southern Ocean from satellite chlorophyll data, *Deep Sea Res., Part I*, *104*, 9–25.

Holm-Hansen, O., and M. Huntley (1984), Feeding requirements of krill in relation to food sources, *J. Crustacean Biol.*, *4*, 156–173.

Huang, K., H. Ducklow, M. Vernet, N. Cassar, and M. L. Bender (2012), Export production and its regulating factors in the West Antarctica Peninsula region of the Southern Ocean, *Global Biogeochem. Cycles*, *26*, GB2005, doi:10.1029/2010GB004028.

Johnson, R., P. G. Strutton, S. W. Wright, A. McMinn, and K. M. Meiners (2013), Three improved satellite chlorophyll algorithms for the Southern Ocean, *J. Geophys. Res. Oceans*, *118*, 3694–3703, doi:10.1002/jgrc.20270.

Jonsson, B. F., S. C. Doney, J. P. Dunne, and M. L. Bender (2013), Evaluation of the Southern Ocean O_2/Ar-based NCP estimates in a model framework, *J. Geophys. Res. Biogeosci.*, *118*, 385–399, doi:10.1002/jgrg.20032.

Kahru, M., and B. G. Mitchell (2010), Blending of ocean colour algorithms applied to the Southern Ocean, *Remote Sens. Lett.*, *1*(2), 119–124.

Kalnay, E., et al. (1996), The NCEP/NCAR 40-year reanalysis project, *Bull. Am. Meteorol. Soc.*, *77*(3), 437–471.

Kavanaugh, M. T., F. N. Abdala, H. Ducklow, D. Glover, W. Fraser, D. Martinson, S. Stammerjohn, O. Schofield, and S. C. Doney (2015), Effect of continental shelf canyons on phytoplankton biomass and community composition along the Western Antarctic Peninsula, *Mar. Ecol. Prog. Ser.*, *524*, 11–26.

King, J. C. (1994), Recent climate variability in the vicinity of the Antarctic Peninsula, *Int. J. Climatol.*, *14*(4), 357–369.

Korb, R. E., M. J. Whitehouse, and P. Ward (2004), SeaWiFS in the Southern Ocean: Spatial and temporal variability in phytoplankton biomass around South Georgia, *Deep Sea Res., Part II*, *51*(1–3), 99–116.

Kortzinger, A., U. Send, R. S. Lampitt, S. Hartman, D. W. R. Wallace, J. Karstensen, M. G. Villagarcia, O. Llinas, and M. D. DeGrandpre (2008), The seasonal pCO_2 cycle at 49°N/16.5°W in the northeastern Atlantic Ocean and what it tells us about biological productivity, *J. Geophys. Res.*, *113*, C04020, doi:10.1029/2007JC004347.

Lannuzel, D., V. Schoemann, J. de Jong, J. L. Tison, and L. Chou (2007), Distribution and biogeochemical behaviour of iron in the East Antarctic sea ice, *Mar. Chem.*, *106*(1–2), 18–32.

Lannuzel, D., V. Schoemann, J. de Jong, L. Chou, B. Delille, S. Becquevort, and J. L. Tison (2008), Iron study during a time series in the western Weddell pack ice, *Mar. Chem.*, *108*(1–2), 85–95.

Laws, E. A., P. G. Falkowski, W. O. Smith, H. Ducklow, and J. J. McCarthy (2000), Temperature effects on export production in the open ocean, *Global Biogeochem. Cycles*, *14*(4), 1231–1246.

Li, Z., and N. Cassar (2016), Satellite estimates of net community production based on O_2/Ar observations and comparison to other estimates, *Global Biogeochem. Cycles*, *30*, 735–752, doi:10.1002/2015GB005314.

Loch, A. (1966), The logarithm in biology 1. Mechanisms generating the log-normal distribution exactly, *J. Theor. Biol.*, *12*(2), 276–290.

Marshall, G. J. (2003), Trends in the Southern Annular Mode from observations and reanalyses, *J. Clim.*, *16*(24), 4134–4143.

Martin, J. H., and R. M. Gordon (1988), Northeast Pacific iron distributions in relation to phytoplankton productivity, *Deep Sea Res., Part I*, *35*(2), 177–196.

Martin, J. H., R. M. Gordon, and S. E. Fitzwater (1990), Iron in Antarctic waters, *Nature*, *345*(6271), 156–158.

Martinson, D. G., S. E. Stammerjohn, R. A. Iannuzzi, R. C. Smith, and M. Vernet (2008), Western Antarctic Peninsula physical oceanography and spatio-temporal variability, *Deep Sea Res., Part II*, *55*(18–19), 1964–1987.

Massom, R. A., et al. (2006), Extreme anomalous atmospheric circulation in the West Antarctic Peninsula region in austral spring and summer 2001/02, and its profound impact on sea ice and biota, *J. Clim.*, *19*(15), 3544–3571.

Mitchell, B. G., and O. Holm-Hansen (1991), Observations and modeling of the Antarctic phytoplankton crop in relation to mixing depth, *Deep Sea Res., Part I*, *38*(8–9), 981–1007.

Mitchell, B. G., E. A. Brody, O. Holm-Hansen, C. Mcclain, and J. Bishop (1991), Light limitation of phytoplankton biomass and macronutrient utilization in the Southern Ocean, *Limnol. Oceanogr.*, *36*(8), 1662–1677.

Moline, M. A., and B. B. Prezelin (2000), Optical fractionation of chlorophyll and primary production for coastal waters of the Southern Ocean, *Polar Biol.*, *23*(2), 129–136.

Montes-Hugo, M., S. C. Doney, H. W. Ducklow, W. Fraser, D. Martinson, S. E. Stammerjohn, and O. Schofield (2009), Recent changes in phytoplankton communities associated with rapid regional climate change along the Western Antarctic Peninsula, *Science*, *323*(5920), 1470–1473.

Moreau, S., B. Mostajir, S. Belanger, I. R. Schloss, M. Vancoppenolle, S. Demers, and G. A. Ferreyra (2015), Climate change enhances primary production in the Western Antarctic Peninsula, *Global Change Biol.*, *21*(6), 2191–2205.

Morel, A., and L. Prieur (1977), Analysis of variations in ocean color, *Limnol. Oceanogr.*, *22*(4), 709–722.

Nelson, D. M., and W. O. Smith (1991), Sverdrup revisited: Critical depths, maximum chlorophyll levels, and the control of Southern Ocean productivity by the irradiance-mixing regime, *Limnol. Oceanogr.*, *36*(8), 1650–1661.

O'Reilly, J. E., S. Maritorena, B. G. Mitchell, D. A. Siegel, K. L. Carder, S. A. Garver, M. Kahru, and C. McClain (1998), Ocean color chlorophyll algorithms for SeaWiFS, *J. Geophys. Res.*, *103*(C11), 24,937–24,953.

Orsi, A. H., T. Whitworth, and W. D. Nowlin (1995), On the meridional extent and fronts of the Antarctic Circumpolar Current, *Deep Sea Res., Part I*, *42*(5), 641–673.

Ostle, C., M. Johnson, P. Landschutzer, U. Schuster, S. Hartman, T. Hull, and C. Robinson (2015), Net community production in the North Atlantic Ocean derived from Volunteer Observing Ship data, *Global Biogeochem. Cycles*, *29*, 80–95, doi:10.1002/2014GB004868.

Palevsky, H. I., P. Quay, D. Lockwood, and D. Nicholson (2016), The annual cycle of gross primary production, net community production, and export efficiency across the North Pacific Ocean, *Global Biogeochem. Cycles*, *30*, 361–380, doi:10.1002/2015GB005318.

Reuer, M. K., B. A. Barnett, M. L. Bender, P. G. Falkowski, and M. B. Hendricks (2007), New estimates of Southern Ocean biological production rates from O_2/Ar ratios and the triple isotope composition of O_2, *Deep Sea Res., Part I*, *54*(6), 951–974.

Rivkin, R. B., and L. Legendre (2001), Biogenic carbon cycling in the upper ocean: Effects of microbial respiration, *Science*, *291*(5512), 2398–2400.

Ross, R. M., L. B. Quetin, D. G. Martinson, R. A. Iannuzzi, S. E. Stammerjohn, and R. C. Smith (2008), Palmer LTER: Patterns of distribution of five dominant zooplankton species in the epipelagic zone west of the Antarctic Peninsula, 1993–2004, *Deep Sea Res., Part II*, *55*(18–19), 2086–2105.

Saba, G., et al. (2014), Winter and spring controls on the summer food web of the coastal West Antarctic Peninsula, *Nat. Commun.*, *5*, 4318–4325.

Sarmiento, J. L., and N. Gruber (2006), *Ocean Biogeochemical Dynamics*, Princeton Univ. Press, Princeton, N. J.

Schofield, O., et al. (2013), Penguin biogeography along the West Antarctic Peninsula: Testing the canyon hypothesis with Palmer LTER observations, *Oceanography*, *26*(3), 204–206.

Smith, R., et al. (1995), The Palmer LTER: A long-term ecological research program at Palmer station, Antarctica, *Oceanography*, *8*(3), 77–86.

Smith, R. C., D. G. Martinson, S. E. Stammerjohn, R. A. Iannuzzi, and K. Ireson (2008), Bellingshausen and Western Antarctic Peninsula region: Pigment biomass and sea-ice spatial/temporal distributions and interannual variability, *Deep Sea Res., Part II*, *55*(18–19), 1949–1963.

Smith, W. O., and D. M. Nelson (1986), Importance of ice edge phytoplankton production in the Southern Ocean, *Bioscience*, *36*(4), 251–257.

Sokolov, S., and S. R. Rintoul (2007), On the relationship between fronts of the Antarctic Circumpolar Current and surface chlorophyll concentrations in the Southern Ocean, *J. Geophys. Res.*, *112*, C07030, doi:10.1029/2006JC004072.

Stammerjohn, S. E., D. G. Martinson, R. C. Smith, and R. A. Iannuzzi (2008a), Sea ice in the Western Antarctic Peninsula region: Spatio-temporal variability from ecological and climate change perspectives, *Deep Sea Res., Part II*, *55*(18–19), 2041–2058.

Stammerjohn, S. E., D. G. Martinson, R. C. Smith, X. Yuan, and D. Rind (2008b), Trends in Antarctic annual sea ice retreat and advance and their relation to El Niño-Southern Oscillation and Southern Annular Mode variability, *J. Geophys. Res.*, *113*, C03S90, doi:10.1029/2007JC004269.

Steinberg, D. K., K. E. Ruck, M. R. Gleiber, L. M. Garzio, J. S. Cope, K. S. Bernard, S. Stammerjohn, O. Schofield, L. B. Quetin, and R. M. Ross (2015), Long-term (1993–2013) changes in macrozooplankton off the Western Antarctic Peninsula, *Deep Sea Res., Part I*, *101*, 54–70.

Tagliabue, A., J. B. Sallee, A. R. Bowie, M. Levy, S. Swart, and P. W. Boyd (2014), Surface-water iron supplies in the Southern Ocean sustained by deep winter mixing, *Nat. Geosci.*, *7*(4), 314–320.

Thompson, A. F., and M. K. Youngs (2013), Surface exchange between the Weddell and Scotia Seas, *Geophys. Res. Lett.*, *40*, 5920–5925, doi:10.1002/2013GL058114.

Thompson, D. W. J., J. M. Wallace, and G. C. Hegerl (2000), Annular modes in the extratropical circulation. Part II: Trends, *J. Clim.*, *13*(5), 1018–1036.

Tortell, P. D., E. C. Asher, H. Ducklow, J. C. Goldman, J. Dacey, J. Grzymski, J. Young, S. Kranz, S. Bernard, and F. Morel (2014), Metabolic balance of coastal Antarctic waters revealed by autonomous pCO_2 and ΔO_2/Ar measurements, *Geophys. Res. Lett.*, *41*, 6803–6810, doi:10.1002/2014GL061266.

Treguer, P., and G. Jacques (1992), Dynamics of nutrients and phytoplankton, and fluxes of carbon, nitrogen and silicon in the Antarctic Ocean, *Polar Biol.*, *12*(2), 149–162.

Vaughan, D. G., G. J. Marshall, W. M. Connolley, C. Parkinson, R. Mulvaney, D. A. Hodgson, J. C. King, C. J. Pudsey, and J. Turner (2003), Recent rapid regional climate warming on the Antarctic Peninsula, *Clim. Change*, *60*(3), 243–274.

Venables, H. J., A. Clarke, and M. P. Meredith (2013), Wintertime controls on summer stratification and productivity at the Western Antarctic Peninsula, *Limnol. Oceanogr.*, *58*(3), 1035–1047.

Vernet, M., D. Martinson, R. Iannuzzi, S. Stammerjohn, W. Kozlowski, K. Sines, R. Smith, and I. Garibotti (2008), Primary production within the sea-ice zone west of the Antarctic Peninsula: I-Sea ice, summer mixed layer, and irradiance, *Deep Sea Res., Part II*, *55*(18–19), 2068–2085.

West, M. (1984), Outlier models and prior distributions in Bayesian linear regression, *J. R. Stat. Soc., Ser. B*, *46*(3), 431–439.

Weston, K., T. D. Jickells, D. S. Carson, A. Clarke, M. P. Meredith, M. A. Brandon, M. I. Wallace, S. J. Ussher, and K. R. Hendry (2013), Primary production export flux in Marguerite Bay (Antarctic Peninsula): Linking upper water-column production to sediment trap flux, *Deep Sea Res., Part I*, *75*, 52–66.

Youngs, M. K., A. F. Thompson, M. M. Flexas, and K. J. Heywood (2015), Weddell Sea export pathways from surface drifters, *J. Phys. Oceanogr.*, *45*(4), 1068–1085.